

# Active Vertical Takeoff of an Aquatic UAV

Étienne Tétreault, David Rancourt and Alexis Lussier Desbiens

**Abstract**—To extend the mission duration of smaller unmanned aerial vehicles, this paper presents a solar recharge approach that uses lakes as landing, charging, and standby areas. The Sherbrooke University Water-Air Vehicle (SUWAVE) is a small aircraft capable of vertical takeoff and landing on water. A second-generation prototype has been developed with new capabilities: solar recharging, autonomous flight, and a larger takeoff envelope using an actuated takeoff strategy. A 3D dynamic model of the new takeoff maneuver is conceived to understand the major forces present during this critical phase. Numerical simulations are validated with experimental results from real takeoffs made in the laboratory and on lakes. The final prototype is shown to have accomplished repeated cycles of autonomous takeoff, followed by assisted flight and landing, without any human physical intervention between cycles.

## I. INTRODUCTION

The many advantages of bigger unmanned aerial vehicles (UAVs) are not always enough to compensate for their high price and complexity of use. On the other hand, one of the main drawbacks of smaller platforms is their short flight duration. Solar panels may mitigate this issue, but at a small scale they are not sufficient to enable continuous flight [1], so there is still the need to land and recharge. Numerous laboratories have developed diverse landing approaches, such as using vertical walls [2]–[5], electric power lines [6], and moving platforms [7]. Another interesting solution is the use of bodies of water, which offer some unique advantages: they form a large flat surface with no obstacle, their location is known, and they are quite common in places like Canada.

An aquatic unmanned aerial vehicle (aquaUAV) can use water as a safe landing spot, but also has its own set of challenges [8]. Seaplanes are the traditional aquatic-aerial platforms. The Oregon Ironworks “SeaScout”, Warrior Aero-marine’s “Gull” and the University of Michigan’s “Flying Fish” are aquaUAVs with autonomous takeoff and landing capabilities [9]–[11]. Those are large aircraft, the lightest having a mass of 18 kg. Numerous problems arise as standard seaplane configurations are scaled down. Waves are a concern for runway takeoff and shallow descent landing [12]. The risk of capsizing while resting on water also increases with smaller size [13]. Multicopters have also been adapted to aquatic operation [14], [15], using vertical takeoff and landing (VTOL) to leave water. However, their range remains shorter than that of their fixed-wing counterpart, though some new designs may mitigate that [16].

This work was supported by FRQNT and NSERC.

The authors are with the Createk Design Lab at the Université de Sherbrooke, Canada, J1K 2R1 {etienne.tetreault, david.rancourt2, alexis.lussier.desbiens}@usherbrooke.ca.

The Sherbrooke University Water-Air Vehicle (SUWAVE) is an aquaUAV with autonomous VTOL and flight capabilities, able to perform a solar recharge between mission cycles (Fig 1). The flying wing design makes for a low profile on water, which prevents capsizing while retaining the endurance characteristic of fixed-wing aircraft. The single propeller can reorient itself to execute vertical takeoff, and water re-entry is done by diving nose-first [13]. Both these maneuvers were implemented to circumvent undesired wave interactions associated with traditional runway takeoffs and landings on water.

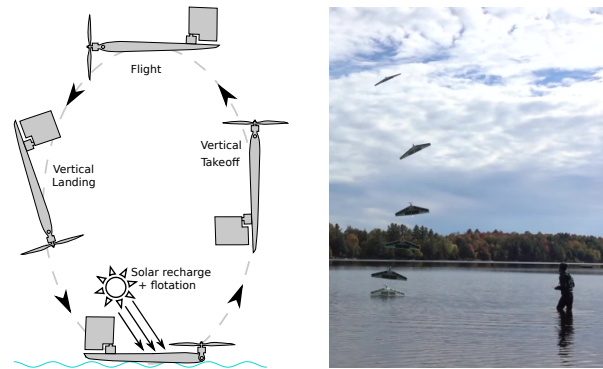


Fig. 1. Proposed mission cycle (left), and time lapse of autonomous takeoff from lake (right).

SUWAVE’s vertical takeoff starts by tilting the propulsion system vertically and applying full thrust so that the nose rapidly rises from the water. This pulls the whole wing out before aligning the two bodies for normal flight. In the earlier prototype, this alignment was performed passively using counterweight and latches. This required a fine balance of gravity, buoyancy and inertial forces for successful takeoffs [13]. This passive strategy was sensitive to wave perturbations and strong wind could prevent the latching of both bodies. This version of the SUWAVE could also only takeoff from water as it needed free space under the wing to allow for the counterweight motion.

The new SUWAVE presented in this paper uses an actuated joint to tilt the propeller. It also includes a rudder and a controller that takes advantage of these two new actuators to orient the SUWAVE during takeoff. Takeoff in wind and from solid ground are now possible with these actuators that are effective even in the first few seconds of takeoff at low airspeed [17]. The propeller tilt and the rudder immersed in the prop wash control pitch and yaw movement respectively, leaving roll rate unchecked. During vertical takeoffs, the spin of the plane around itself does not affect the trajectory and

the thrust is aligned to fight gravity without the need for aerodynamical lift. This vertical trajectory is maintained until sufficient airspeed and altitude are reached. Then, a transition phase smoothly brings the nose down to transition to normal level flight.

The main contribution of this paper consists in the new SUWAVE prototype and actuated takeoff strategy to perform robust vertical takeoffs, as opposed to the preceding passive approach. The new configuration allows the SUWAVE to takeoff vertically from water or land. Another contribution of this paper is the extension of the 2D takeoff model presented in [13] to explain the undesirable gyroscopic effects caused by the rapid tilt actuation. The structure of this paper reflects those novelties. Section II presents the new aircraft, with the avionics and the actuators required for autonomous active takeoff. The Section III describe the 3D numeric model used to represent the new takeoff sequence while the controller for this maneuver is explained in Section IV. Lastly, the paper presents some experimental results demonstrating the new autonomous vertical capabilities of the prototype in Section V. Those results are also demonstrated in the attached video.

## II. PROTOTYPE VEHICLE

Compared to the first generation of SUWAVE, the new model is larger and heavier, mostly due to the added solar panels, protective fiberglass and avionics required for autonomous flight. Fig. 2 depicts the aircraft, and Table I presents its mass budget.

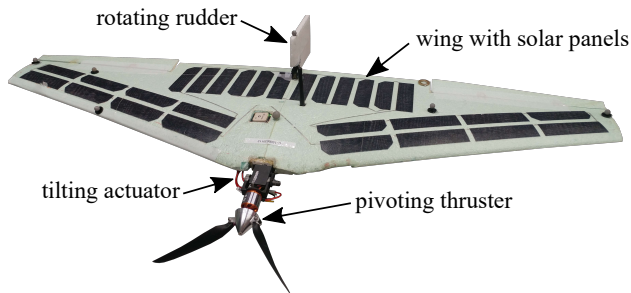


Fig. 2. Global view of the second-generation SUWAVE prototype.

TABLE I  
SUWAVE'S MASS BUDGET

<b>Empty aircraft:</b> Foam, solar panels, fiberglass, epoxy, 4 x RC servomotors	404 g
<b>Propulsion:</b> Motor 300 W, and folding propeller 12 x 6	117 g
<b>Battery:</b> 3S-1000 mAh	90 g
<b>Avionic:</b> Autopilot board, ESC 30 A, RC receiver, Telemetry and GPS antenna	129 g
<b>Other</b>	125 g
<b>Total mass, solar SUWAVE</b>	<b>865 g</b>

### A. Airframe Configuration

The aircraft has a total mass of 865 g and a wingspan of 1240 mm. Its main feature is the tilt mechanism on the nose, which is activated by an RC servomotor and used to tilt the propeller up or down. In the previous generation, this pivot was a free hinge that passively rotated under its own weight [13]. The new actuated version enables control of the thrust orientation in order to generate the pitching moment and correct the aircraft's attitude. We also added a rudder to the flying wing. By being immersed in the air flow induced by the propeller (prop wash), the rudder can effectively control yaw movement during the initial low airspeed of takeoff.

### B. Electronics and Power Systems

SUWAVE has its own custom autopilot board, derived from the Pixhawk® open standards autopilot [18] with added solar recharge capabilities. With good solar exposure, the charging current is 1.5 A. The flight stack is the open-source PX4 [19], which was also modified to include solar recharge, VTOL from water, and control of the new actuators. The autopilot includes an inertial measurement unit (IMU) and the software performs the necessary sensor fusion to estimate the attitude, position, and velocity of the aircraft. The autopilot and all other sensitive electronics are coated in a waterproof conformal coating.

## III. TAKEOFF MODEL

The new generation of SUWAVE is almost 50% heavier than its predecessor, with a very different mass distribution. This causes the two versions to have very distinct trajectories while using a similar takeoff strategy. The takeoffs of the new active and solar version are much more tridimensional, and the path taken is no longer held in a single plane. One of the main challenges is the high positive yaw rate occurring once the aircraft fully elevates its nose. Without a rudder, this uncontrolled movement leads to takeoff failure. To understand the origin of this dynamic phenomenon, we developed a 3D model which we used to validate the effectiveness of the rudder to counter this undesired movement. The various bodies, forces, and points of interest of the model are shown in Fig. 3.

### A. Reference Frames, Bodies and Motion

The various frames and their orientation follow aeronautical standards [20]. The model uses three of them: the inertial frame  $\mathcal{N}$ , and two others affixed to the rigid bodies of the flying wing  $\mathcal{W}$  and thruster  $\mathcal{P}$  respectively. The inertial frame  $\mathcal{N}$  is of type north-east-down (NED), meaning that its  $x$  axis points north,  $y$  points east, and  $z$  points vertically downward. Its origin is named  $\mathcal{N}_0$ . The flying wing  $\mathcal{W}$  rigid body has its origin at its center of mass,  $\mathcal{W}_{cm}$ . From there, the body  $x$  axis points toward the nose of the aircraft, the  $y$  points toward the starboard wing (the right-hand wing when viewed from the rear), and the  $z$  exits the plane through its belly. This body is free to move in the 3D space and has then 6 degrees of freedom (DOF). The thruster, composed of the brushless

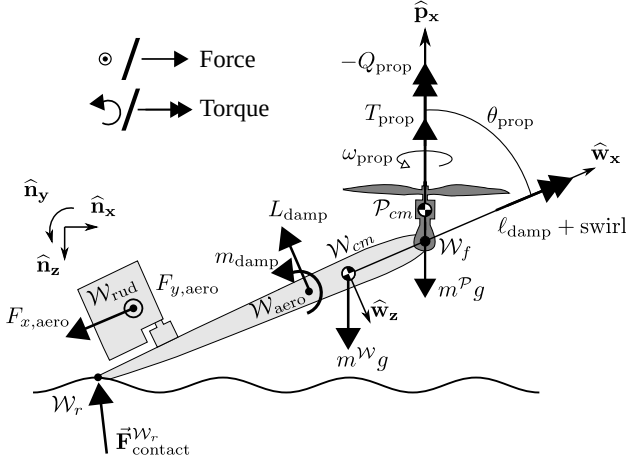


Fig. 3. Free body diagram used in the 3D dynamic takeoff model.

TABLE II  
STATE VARIABLES OF THE FLYING WING

Position	$\vec{r}^{W_{cm}/N_0} = x\hat{n}_x + y\hat{n}_y + z\hat{n}_z$
Attitude	${}^N\mathbf{q}^W = q_0 + q_1\hat{n}_x + q_2\hat{n}_y + q_3\hat{n}_z$
Translation velocity	${}^N\vec{v}^{W_{cm}} = u\hat{w}_x + v\hat{w}_y + w\hat{w}_z$
Angular velocity	${}^N\vec{\omega}^W = p\hat{w}_x + q\hat{w}_y + r\hat{w}_z$

motor and the propeller, forms the second massive body  $\mathcal{P}$ . Its  $x$  axis is aligned with the spin axis of the motor. The propeller is approximated as a rotating disc that spins along that axis with an angular rate of  $\omega_{prop}$ . The thruster  $\mathcal{P}$  can tilt by an angle  $\theta_{prop}$  around the  $y$  axis of the plane. Both  $\omega_{prop}$  and  $\theta_{prop}$  are imposed in simulation.

### B. State Variables and Motion Equations

The choice of state variables also follows the aeronautical norm. There are 13 of them, split into four groups as follows. 1) The position states  $\vec{r}^{W_{cm}/N_0} = x\hat{n}_x + y\hat{n}_y + z\hat{n}_z$  relate the wing's center of mass to the inertial origin and are expressed in inertial components. 2) The angular position states  ${}^N\mathbf{q}^W = q_0 + q_1\hat{n}_x + q_2\hat{n}_y + q_3\hat{n}_z$  are in the quaternion that describes the rotation of the  $\mathcal{P}$  frame in the inertial frame  $\mathcal{N}$ . The quaternion representation is favored over the usual Euler angles for multiple reasons: it does not have a singularity for  $90^\circ$  elevation; it does not rely on trigonometric functions, which is computationally efficient; and it is readily available in the Px4 firmware. 3) The translation velocity states  ${}^N\vec{v}^{W_{cm}} = u\hat{w}_x + v\hat{w}_y + w\hat{w}_z$  are the velocity of the wing center of mass in the inertial frame, expressed along the wing's axis. Because there is no wind in the current model, this velocity is equivalent to the airspeed. 4) The angular velocity states  ${}^N\vec{\omega}^W = p\hat{w}_x + q\hat{w}_y + r\hat{w}_z$  are also expressed in the wing frame  $\mathcal{P}$ . Those three last variables are respectively called the roll, pitch, and yaw rates of the aircraft. Together, the thirteen state variables are used to describe the vehicle motion and form the unknowns solved by the equations of motion. Table II summarizes them.

For the system of 13 states and 6 DOF, 13 differential equations are required. Seven equations come from the classic

kinematic equations [20] as follows

$$\begin{bmatrix} \dot{x} \\ \dot{y} \\ \dot{z} \end{bmatrix} = \begin{bmatrix} q_0^2 + q_1^2 - q_2^2 - q_3^2 & 2(q_1q_2 - q_0q_3) & 2(q_1q_3 + q_0q_2) \\ 2(q_1q_2 + q_0q_3) & q_0^2 + q_2^2 - q_1^2 - q_3^2 & 2(q_2q_3 - q_0q_1) \\ 2(q_1q_3 - q_0q_2) & 2(q_2q_3 + q_0q_1) & q_0^2 + q_3^2 - q_1^2 - q_2^2 \end{bmatrix} \begin{bmatrix} u \\ v \\ w \end{bmatrix}, \quad (1)$$

$$\begin{bmatrix} \dot{q}_0 \\ \dot{q}_1 \\ \dot{q}_2 \\ \dot{q}_3 \end{bmatrix} = \begin{bmatrix} 0 & -p & -q & -r \\ p & 0 & r & -q \\ q & -r & 0 & p \\ r & q & -p & 0 \end{bmatrix} \begin{bmatrix} q_0 \\ q_1 \\ q_2 \\ q_3 \end{bmatrix}. \quad (2)$$

Six remaining equations are obtained from the dynamic equations. Because the thruster  $\mathcal{P}$  moves about the wing  $\mathcal{W}$  with a predetermined motion, and the reaction forces are not needed, D'Alembert's principle is used. For a system  $\mathcal{S}$  composed of the bodies  $\mathcal{W}$  and  $\mathcal{P}$ , the resultant forces  $\vec{F}^S$  and moments  $\vec{M}^{S/W_{cm}}$  about  $W_{cm}$  are equal to the corresponding effective forces  ${}^N\vec{F}^S$  and moments  ${}^N\vec{M}^{S/W_{cm}}$ . The equations thus formed are

$$\vec{F}^S = m^W * {}^N\vec{a}^{W_{cm}} + m^P * {}^N\vec{a}^{P_{cm}}, \quad (3)$$

$$\vec{M}^{S/W_{cm}} = \frac{{}^N d {}^N\vec{H}^{S/W_{cm}}}{dt} + {}^N\vec{v}^{W_{cm}} \times {}^N\vec{L}^S, \quad (4)$$

where  ${}^N\vec{H}^{S/W_{cm}}$  and  ${}^N\vec{L}^S$  are respectively the angular and linear momentum of the system, while  ${}^N\vec{v}^{W_{cm}}$  is the velocity of  $W_{cm}$ . The six scalar equations needed are produced by extracting the  $\hat{w}_x$ ,  $\hat{w}_y$ , and  $\hat{w}_z$  components of each of these two vectorial equations. These equations are generated automatically using MotionGenesis™ [21]. Equations (1-4) are solved for in Matlab™.

### C. Forces

The various forces modeled are described below.

1) *Gravity*: The force of gravity is applied to the center of mass of the two bodies and points directly downward, in the  $\hat{n}_z$  direction. The values used for  $m^W$  and  $m^P$  were 730 g and 135 g respectively.

2) *Motor thrust, torque and angular speed*: The static thrust, torque, and angular speed of the motor and propeller duo were measured experimentally using a dynamometer [22] and are presented in Fig. 4. Those measurements are directly used as inputs in the numerical model as the forward velocity  $u$  remains low throughout takeoff simulations (i.e., the advance ratio  $J$  remains below 0.05). Ground effects with the water surface are also neglected, with limited effects on the simulated trajectories, because of the limited time spent in close proximity to the water. The thrust  $T_{prop}$  is applied through the propeller's center of mass, and the motor torque  $Q_{prop}$  is applied directly to the flying wing. The angular rate of the propeller  $\omega_{prop}$  is modeled as a first-order step response. This rotation, when combined with the propeller's inertia calculated from CAD software, generates the undesirable gyroscopic effects. The quantities  $T_{prop}$ ,  $Q_{prop}$ , and  $\omega_{prop}$  are all oriented along the thruster spin axis  $\hat{p}_x$ .

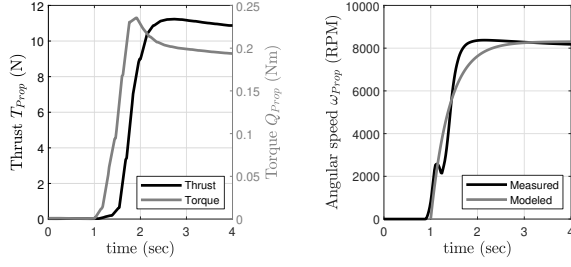


Fig. 4. From the static propeller test: measured thrust and torque (left), measured angular velocity and first-order response modeled (right).

3) *Contact with water*: The interactions of the wing with water are simplified as contact forces on three points of the wing  $\mathcal{W}$ : the front  $\mathcal{W}_f$ , the trailing edge right corner  $\mathcal{W}_r$ , and its counterpart on the left  $\mathcal{W}_l$ . On each of these points, three contact forces are combined to form  $\vec{\mathbf{F}}_{\text{contact}}$  when they are in contact with the surface. First, the buoyancy is modeled as a variable stiffness spring in the  $\hat{\mathbf{n}}_z$  direction. Its force varies linearly with the depth of the application point. As the plane leaves the water, the portion of immersed wing decreases, as does the buoyancy force. To represent this, the ratio of submerged root chord  $n_{\text{chord}}$ , ranging from 0 to 1, is calculated and used to reduce the stiffness of the spring. The stiffness is maximum when the plane lies flat, its chord being fully immersed ( $n_{\text{chord}} = 1$ ). It diminishes once the nose rises and tends toward zero as the trailing edge leaves the water ( $n_{\text{chord}} = 0$ ). Buoyancy keeps the aircraft on the water's surface before takeoff. To model the drag produced by water on the wing, two more contact forces proportional and opposed to the velocity of their application point are added. These damping forces are set along the aircraft's axes  $\hat{\mathbf{w}}_z$  and  $\hat{\mathbf{w}}_x$ . The force about  $\hat{\mathbf{w}}_z$  has the highest damping coefficient and represents the penetration of the wing into the water. It stabilizes the initial oscillations of the aircraft while it rests on water. The damping about  $\hat{\mathbf{w}}_x$  is the skin friction between the water and the wing. It counters the motor torque, reducing the initial yaw rotation while the plane is still in the water. The resulting force is applied on each of the three contact points and its equation for a generic point  $\mathcal{W}_i$  is

$$\vec{\mathbf{F}}_{\text{contact}}^{\mathcal{W}_i} = -n_{\text{chord}}k_{\text{water}}(\vec{\mathbf{r}}^{\mathcal{W}_i}/N_0, \hat{\mathbf{n}}_z)\hat{\mathbf{n}}_z - c_{\text{pen}}(\mathcal{N}\vec{\mathbf{v}}^{\mathcal{W}_i}, \hat{\mathbf{w}}_z)\hat{\mathbf{w}}_z - c_{\text{skin}}(\mathcal{N}\vec{\mathbf{v}}^{\mathcal{W}_i}, \hat{\mathbf{w}}_x)\hat{\mathbf{w}}_x. \quad (5)$$

where  $c_{\text{skin}}$  and  $c_{\text{pen}}$  are the damping coefficients while  $k_{\text{water}}$  is the maximum spring stiffness. They are the only coefficients adjusted empirically to fit experimental data and are related to the airplane geometry. The values used in the model are  $c_{\text{skin}} = 0.23$  Ns/m,  $c_{\text{pen}} = 2.7$  Ns/m and  $k_{\text{water}} = 100$  N/m.

4) *Aerodynamic Forces*: The model developed is interested only in the first few seconds of takeoff, characterized by low airspeed. By the end of the simulation, the advance velocity  $u$  of the aircraft is about 2 m/s, compared to its cruising speed of 10 m/s. Aerodynamic forces such as lift, drag, and those produced by the elevons are thus not included. However, simulations with only the thruster forces

and gravity showed three important differences with experimental results: the motor's torque continuously increased the roll rate, the rudder's stabilising effect on yaw was absent, and there was a lack of pitch rate damping. Three aerodynamic effects were thus added to the model to resolve these issues.

First, the swirl of the propeller slipstream was added to counteract the motor torque and limit the roll rate. As per [23], the swirl is not modeled explicitly. It is rather represented as a positive rolling moment that opposes the torque applied by the thruster on the airframe. The value of this moment is about 60% of the  $\hat{\mathbf{w}}_x$  component of the motor torque.

Second, to represent the yaw correction of the rudder, the lift and drag due to the prop wash were included. To do so, the rudder is considered as a flat plate immersed in a purely axial slipstream from the propeller [23]. The airspeed perceived by this surface is then

$$\vec{\mathbf{v}}_{\text{rel}} = \mathcal{N}\vec{\mathbf{v}}^{\mathcal{W}_{cm}} + \mathcal{N}\vec{\boldsymbol{\omega}}^{\mathcal{W}} \times \vec{\mathbf{r}}^{\text{Rud}/\mathcal{W}_{cm}} + V_{\text{prop}}\hat{\mathbf{w}}_x, \quad (6)$$

where  $V_{\text{prop}}$  is the airspeed induced by the prop wash on the rudder and has been measured to be 10 m/s with an anemometer in static conditions. The prop wash airspeed is considered constant throughout the simulation because the advance ratio of the propeller remains near zero. The lift and drag coefficients of the rudder are those from the flat-plate theory [2] and are written as

$$\beta_{\text{rel}} = \text{atan2}(\vec{\mathbf{v}}_{\text{rel}} \cdot \hat{\mathbf{w}}_y, \vec{\mathbf{v}}_{\text{rel}} \cdot \hat{\mathbf{w}}_x), \quad (7)$$

$$\alpha = \beta_{\text{rel}} - \delta_{\text{rud}}, \quad (8)$$

$$C_L = 2 \sin(\alpha) \cos(\alpha), \quad (9)$$

$$C_D = 2 \sin^2(\alpha), \quad (10)$$

where  $\beta_{\text{rel}}$  is the sideslip angle at the rudder,  $\delta_{\text{rud}}$  is the rudder's deflection as commanded by the controller, and  $\alpha$  is the resulting angle of attack. The standard lift and drag formulas are converted to  $x$  and  $y$  forces along the aircraft's axis for convenience, using

$$F_{y,\text{aero}} = \frac{1}{2}\rho S_{\text{rud}}|\vec{\mathbf{v}}_{\text{rel}}|^2 (C_L \sin \beta_{\text{rel}} - C_D \cos \beta_{\text{rel}}), \quad (11)$$

$$F_{x,\text{aero}} = \frac{1}{2}\rho S_{\text{rud}}|\vec{\mathbf{v}}_{\text{rel}}|^2 (-C_L \cos \beta_{\text{rel}} - C_D \sin \beta_{\text{rel}}), \quad (12)$$

where  $\rho$  is the air density and  $S_{\text{rud}} = 0.013$  m<sup>2</sup> is the rudder's area. Those forces are applied at the aerodynamic center of the rudder located at its quarter-chord and allow the controller to correct the yaw error. They also stabilize the yaw and roll rates of the aircraft.

Third, aerodynamic pitch and roll damping were added. To keep the simulation as simple as possible, only the stability coefficients related to the aircraft's angular speed that also oppose the roll and pitch movement were selected. They are the roll-damping derivative  $C_{\ell, \bar{p}}$ , the pitch-damping derivative  $C_{m, \bar{q}}$ , and the lift-to-pitch-rate derivative  $C_{L, \bar{q}}$ . The force and moments produced by these coefficients are

proportional to the pitch and roll rates they oppose. They are important in this simulation, because of the high angular rates experienced at the start of vertical takeoff. By definition, the chosen derivative coefficients multiply the traditional dimensionless roll rate and pitch rate, respectively defined as

$$\bar{p} = \frac{pb_w}{2V} \quad \text{and} \quad \bar{q} = \frac{q\bar{c}_w}{2V}, \quad (13)$$

where  $b_w$  is the wingspan (1.2 m),  $\bar{c}_w$  is the mean chord of the wing (0.25 m) and  $V$  is the airspeed magnitude. The aerodynamic force and moments produced by the coefficients are the damping components of the roll moment  $l$ , pitch moment  $m$ , and lift  $L$ . Substituting the dimensionless angular rates (13), the formulas for the selected aerodynamic effects become

$$l_{\text{damp}} = \frac{1}{2}\rho V^2 S_w b_w C_{l,\bar{p}} \bar{p} = \frac{1}{4}\rho V S_w b_w^2 C_{l,\bar{p}} p, \quad (14)$$

$$m_{\text{damp}} = \frac{1}{2}\rho V^2 S_w \bar{c}_w C_{m,\bar{q}} \bar{q} = \frac{1}{4}\rho V S_w \bar{c}_w^2 C_{m,\bar{q}} q, \quad (15)$$

$$L_{\text{damp}} = \frac{1}{2}\rho V^2 S_w C_{L,\bar{q}} \bar{q} = \frac{1}{4}\rho V S_w \bar{c}_w C_{L,\bar{q}} q, \quad (16)$$

where  $S_w$  is the wing area (0.298 m<sup>2</sup>). The arrangement of these equations highlights the lesser role played by airspeed  $V$  and the importance of the wingspan  $b_w$  and the mean chord  $\bar{c}_w$ . The values of the three required coefficients were derived from a 3D model of the aircraft in the XFLR5 plane analysis software [24]. They are  $C_{l,\bar{p}} = -0.4$ ,  $C_{m,\bar{q}} = -1.2$  and  $C_{L,\bar{q}} = 5$ .

#### D. Model Validation and Analysis

To validate the model, vertical takeoffs with a physical prototype were conducted. A 3-m diameter pool was installed in a room equipped with Vicon motion-capture cameras. The ceiling height was 6 m above the starting point, limiting recording to the first seconds of the vertical rising sequence. Nets suspended from the ceiling surrounded the pool and served to catch the aircraft. At the end of the vertical manoeuvre, the aircraft stopped its motor and rapidly lowered its nose to fall into the nets. Data acquired by six cameras at a frequency of 200 Hz was analysed to extract the motion of the main wing of the aircraft. Takeoffs from water, hard surfaces, and inclined planes were conducted and recorded. A 3D representation of water takeoff, comparing recorded results to simulated ones is found in Fig. 5. The altitude, orientation and timing are very similar in each case, but there is a slight offset in the  $x$  position.

To ensure the validity of the model over different cases, takeoffs from water were performed with and without the use of the controlled rudder. Kinematic measurements from these two trials and their comparison to simulations are presented in Fig. 6. The error angles  $\Delta\text{pitch}_{y zx}$  and  $\Delta\text{yaw}_{y zx}$  are the angular movements the aircraft must execute to reach a perfectly vertical state, as explained in Section IV.

Good agreement between the model and reality can be observed from these results. The rudder's importance in keeping the aircraft's nose vertical is made clear by looking at the graphics of yaw error  $\Delta\text{yaw}_{y zx}$  and yaw rate  $r$ .

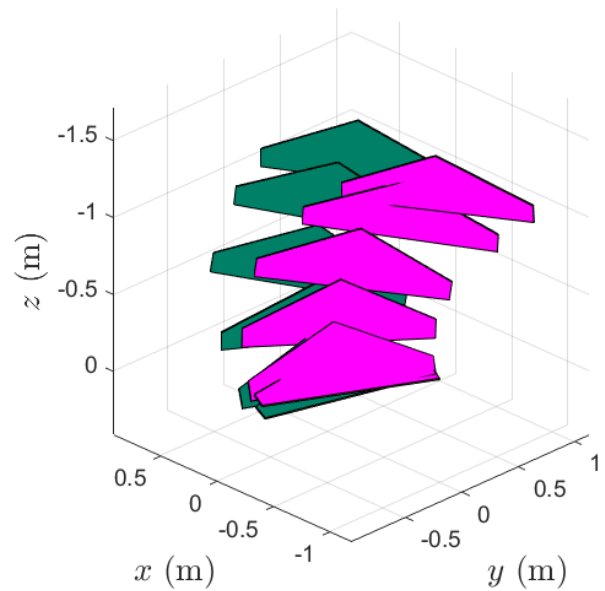


Fig. 5. 3D representation of takeoff, from experimental (pink) and simulated (green) results. Frames are spaced by 0.25 s.

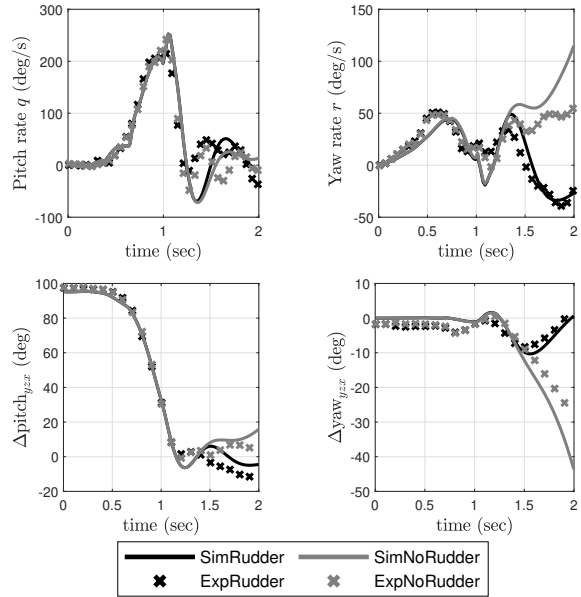


Fig. 6. Comparison of simulated and experimental results, with and without the rudder.

Without the rudder (in gray), large swings in yaw rate occur as the aircraft tilts its nose to control pitch, which become ultimately uncontrollable. In outdoor takeoffs, this leads to the plane executing a complete arc trajectory on its side and diving back down into the lake. The rudder has enough control authority to impose a negative yaw movement and keep the yaw error low. The pitch rate and pitch error are not strongly affected by the rudder, and the latter remains within an acceptable range.

The model helps to understand the dynamics behind the strong positive yaw rate occurring during the vertical takeoff. Two sources of gyroscopic perturbation are included in the model: the spinning propeller and the initial yaw movement

caused by the motor torque. Fig. 7 illustrates results from simulations made by switching off one or both of these effects, to isolate the main contributor to the undesired yaw. In those simulations, yaw correction from the rudder is also excluded, to emphasize the natural motion of the aircraft. The case with both effects omitted leads to an ideal takeoff, where the aircraft rises perfectly vertically without momentum being transferred between its axes. With only the motor torque and the initial yaw movement, the plane ends up with a negative yaw rate. With only the spinning propeller and no initial yaw movement, the plane ends with positive yaw rate. The realistic case, combining both these effects, ends up with the observed positive yaw movement, implying that the gyroscopic effects of the propeller are dominant.

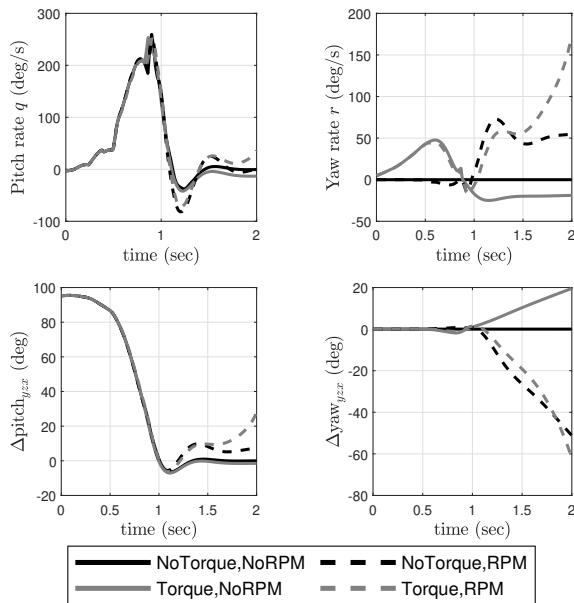


Fig. 7. Simulated effect of motor torque and propeller spin on the induced yaw rate.

#### IV. TAKEOFF CONTROL LAWS

The takeoff is split into two phases: a purely vertical climb, and then a smooth lowering of the nose to level flight. For simplicity, the duration of each phase is fixed with a simple delay, but the airspeed or altitude measurements could be used in future revisions. The control laws are similar for both phases. What differentiates each phase is the desired attitude. The value of their respective control gains are also different, reflecting the specific requirements of each phase and the choice of actuators used.

##### A. Control Laws

Quaternion representation is used for the attitude of the aircraft to avoid singularities. Three frames are used in the controller: the inertial frame  $\mathcal{N}$ , the current frame of the flying wing  $\mathcal{W}$ , and the desired frame  $\mathcal{D}$ . With that in mind, an error quaternion  ${}^{\mathcal{W}}\mathbf{q}^{\mathcal{D}}$  linking the current attitude to the desired one is calculated by

$${}^{\mathcal{W}}\mathbf{q}^{\mathcal{D}} = {}^{\mathcal{W}}\mathbf{q}^{\mathcal{N}} \otimes {}^{\mathcal{N}}\mathbf{q}^{\mathcal{D}} = ({}^{\mathcal{N}}\mathbf{q}^{\mathcal{W}})^{-1} \otimes {}^{\mathcal{N}}\mathbf{q}^{\mathcal{D}}, \quad (17)$$

where the symbol  $\otimes$  is for the quaternion multiplication while the inverse of a quaternion  ${}^{\mathcal{N}}\mathbf{q}^{\mathcal{W}}$  is denoted  $({}^{\mathcal{N}}\mathbf{q}^{\mathcal{W}})^{-1}$  and is equivalent to  ${}^{\mathcal{W}}\mathbf{q}^{\mathcal{N}}$ . The convention of placing the frames as superscript on either side of the quaternion is a notation borrowed from rotation matrices and is used in the same manner. The controller then transforms the quaternion error into three Euler angle errors, which represent the successive rotations required by the aircraft to reach the desired attitude. Mathematically, this requires first converting the quaternion to the unique equivalent rotation matrix represented by the operator  $R_q(\mathbf{q})$ , defined by

$$\begin{aligned} {}^{\mathcal{W}}R^{\mathcal{D}} &= R_q({}^{\mathcal{W}}\mathbf{q}^{\mathcal{D}}) \\ &= \begin{bmatrix} q_0^2 + q_1^2 - q_2^2 - q_3^2 & 2(q_1q_2 - q_0q_3) & 2(q_1q_3 + q_0q_2) \\ 2(q_1q_2 + q_0q_3) & q_0^2 + q_2^2 - q_1^2 - q_3^2 & 2(q_2q_3 - q_0q_1) \\ 2(q_1q_3 - q_0q_2) & 2(q_2q_3 + q_0q_1) & q_0^2 + q_3^2 - q_1^2 - q_2^2 \end{bmatrix}. \end{aligned} \quad (18)$$

The error angles are then extracted from the rotation matrix with the operator  $\mathbf{u}_{yzx}(R)$ , where the subscript  $yzx$  represents the choice of sequence and may change. The specific formula for a  $\mathbf{u}_{yzx}(R)$  transform from the error quaternion  ${}^{\mathcal{W}}\mathbf{q}^{\mathcal{D}}$  is

$$\begin{bmatrix} \Delta\text{pitch}_{yzx} \\ \Delta\text{yaw}_{yzx} \\ \Delta\text{roll}_{yzx} \end{bmatrix} = \mathbf{u}_{yzx}(R_q({}^{\mathcal{W}}\mathbf{q}^{\mathcal{D}})) = \begin{bmatrix} \text{atan2}(-r_{31}, r_{11}) \\ \text{asin}(r_{21}) \\ \text{atan2}(-r_{23}, r_{22}) \end{bmatrix}, \quad (19)$$

where  $r_{ij}$  indicates a single element of the matrix in eq. 18. Each error is used in three independent decoupled control laws controlling the elevons, the propeller tilting and the rudder respectively. A typical control law, with pitch error used as example is

$$\mu_{\text{pitch}} = K_{p,\text{pitch}}\Delta\text{pitch}_{yzx} - K_{d,\text{pitch}}q, \quad (20)$$

where  $\mu_{\text{pitch}}$  is the command,  $K_{p,\text{pitch}}$  and  $K_{d,\text{pitch}}$  are controller gains for this specific loop, and  $q$  is the angular rate associated with this axis to damp the motion. The same controller structure is used for the other two error angles and the first two custom control phases at takeoff, with modifications to the gains to reflect changing aerodynamics conditions. The angular rates are direct measurements from the IMU to avoid numerical differentiation. This simple controller is easy to implement in the PX4 software while being sufficient to make successful takeoffs. The gains were easily tuned empirically, with a trial and error approach. Takeoffs were conducted with all  $K_d$  gains set to zero, to adjust the  $K_p$  gains for a satisfactory response. The  $K_d$  gains were then introduced to add damping and reduce overshoot.

##### B. Takeoff Phase 1: Rising from the Water

This phase marks the transition between the standby state on the water and vertical takeoff. The attitude commanded is an elevation of  $90^\circ$  without consideration for heading. The transformation to Euler angle errors is based on the  $yzx$  sequence presented in eq. 19. It allows for  $\Delta\text{pitch}_{yzx} > 90^\circ$ ,

and because the  $\Delta\text{roll}_{y,z,x}$  is the last angle corrected, it can be excluded and the controller will still keep the nose of the aircraft fully vertical.

### C. Takeoff Phase 2: Transitioning to Climbing

This phase marks the transition between the vertical rise and the climbing state. The attitude commanded is an exponential decrease in elevation from straight up ( $90^\circ$ ) to steady climb ( $15^\circ$ ), with zero bank angle and using the heading at the start of this phase. For smooth transition between controllers, the starting desired attitude of the second phase is the same as in the first phase. The transformation to Euler angle errors is based on the  $y,x,z$  sequence. Because the desired attitude has the same heading as the current one, it is essentially a nose-down movement and once again, the last angle error  $\Delta\text{yaw}_{y,x,z}$  is not used. This phase ends with the aircraft in standard climbing attitude before the Px4 controller takes over.

## V. RESULTS

Experiments have been conducted to confirm some of the new capabilities of SUWAVE's controlled vertical takeoff.

### A. Indoor Takeoffs from Rigid Inclined Planes

The previous generation of SUWAVE required free space under the aircraft to allow for the counterweight's movement at takeoff. Takeoff was then only possible from water. The present model, with its thruster mounted on a servomotor, can orient its propeller and takeoff even from a flat surface. Tests were conducted indoors with the same motion-capture environment used to validate the numeric model. Instead of a pool, the airplane's initial position was flat on a hard surface, with various inclinations used to test the controller's limits. In that spirit, the controller gains used for those tests were the same as the aquatic ones even if it is possible to adjust the controller for better ground takeoff performance. Experimental results comparing takeoffs from various surfaces are shown in Fig. 8, which highlights two types of controller response: converging (gray) and oscillating (black).

One of the main differences during takeoff from hard surfaces is the high pitch rate observed in the first nose-up movement. The cases starting from a  $-30^\circ$  and  $0^\circ$  inclined plane reached a peak of almost 400 deg/s, and the controller, adjusted for a lower velocity, had difficulty dampening the pitch oscillations that followed. Those same oscillations were also transferred in yaw. In the case starting from a  $+30^\circ$  inclined plane, the initial pitch error was far smaller, leading to lower pitch rate with a maximum of 200 deg/s. In fact, despite the difference in initial elevation, the pitch rate in this situation was almost identical to the one from aquatic takeoff. Consequently, the controller gains for water usage were appropriate and both takeoffs had good controller response. The angular velocities and the attitude errors were smaller than their equivalents from the  $-30^\circ$  and  $0^\circ$  inclined plane.

The cases with high pitch rate exhibited greater overshoot and longer settling time, but these did not necessarily mean failed takeoffs. The pitch is still converging to the

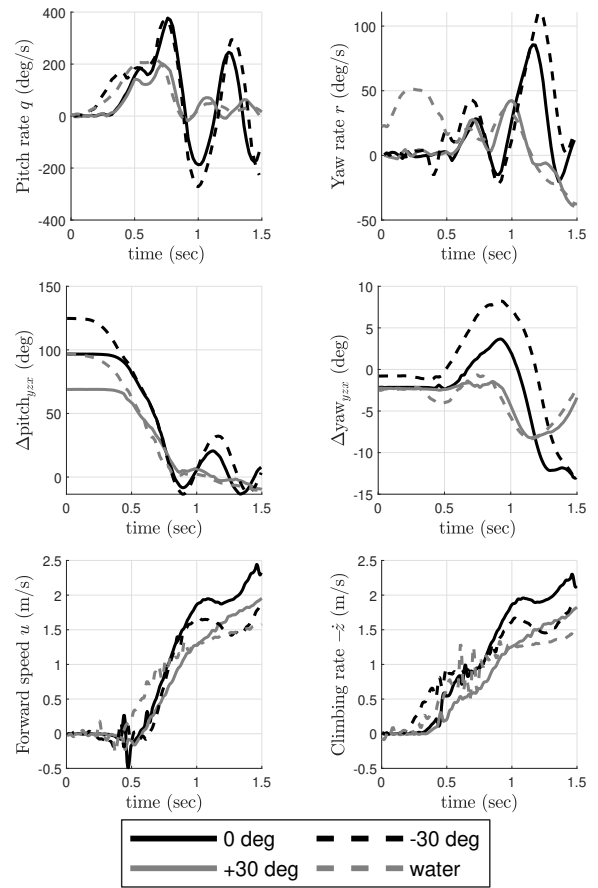


Fig. 8. Indoor takeoffs from various surfaces.

desired value while the yaw error is reasonable. Furthermore, forward speed and climbing rate never ceased to increase, augmenting control authority and bringing the aircraft closer to flight. Outside takeoffs, with enough space to switch to flight will have to be conducted. Nevertheless, the varying controller responses to the initial pitch and pitch rate highlights the sensitivity of the simple controller used with fixed gains.

### B. External Autonomous Takeoffs and Consecutive Flights

Multiple sequential autonomous takeoffs and short flights were conducted on an outdoor lake. This kind of extended takeoff was impossible in an indoor setting due to lack of space. The external tests validated the second phase of the custom controller and the transition to the standard PX4 control for flight. Data acquired by the autopilot during a complete external takeoff are shown in Fig. 9, with the two phases of the custom controller identified. Agreement between the real and the commanded elevation angle can be observed. The steady increase in altitude followed by its stabilization for flight is also presented.

A sequence of three consecutive missions was conducted without human physical contact with the drone. Each mission was composed of an aquatic autonomous takeoff followed by brief loitering and a dive landing in water, both performed through manual control with a radio transmitter. After a short

rest on water, SUWAVE would repeat the takeoff and flight. GPS recordings of the three flights are presented in Fig. 10.

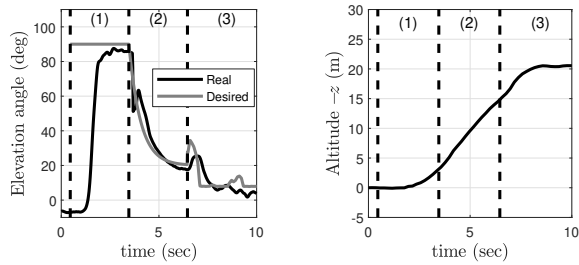


Fig. 9. Vertical takeoff from lake and transition to flight with three controller sequences: (1) rising, (2) climbing, and (3) PX4.



Fig. 10. GPS tracking of three consecutive missions, with full autonomous takeoff and no physical intervention between flights.

## VI. CONCLUSION

The main contribution of this project is a new version of SUWAVE with added capabilities. The aircraft itself was reworked to include the avionics required for autonomous flight and solar recharge. More importantly, the developed version now executes an autonomous and active vertical takeoff using new actuators with their associated control law. The new active version has a larger takeoff envelope compared to the previous passive approach, driven by gravity. Another contribution of this project was the creation of a numerical 3D model of the vertical takeoff from water. It was used to identify the gyroscopic effect from the spinning propeller as the source of the undesired yaw rate occurring at takeoff.

Important results include the autonomous takeoff and the new ability to start missions from water, hard ground, or an inclined plane. We performed takeoff experiments in a motion capture room for data acquisition, and conducted successful external takeoffs that led to flight. The ability to execute consecutive sequences of takeoff, flight, landing, and rest—all without physical intervention—was also demonstrated.

The next steps of the project involve performing consecutive missions with solar recharging while resting on a lake between flights. It may also be advantageous to investigate using two sets of tilting propellers, because in

such a configuration, the torque and gyroscopic effect from the propellers would cancel out.

## REFERENCES

- [1] N. André, “Design of solar powered airplanes for continuous flight,” *DISS ETH*, 2008.
- [2] R. Cory and R. Tedrake, “Experiments in fixed-wing uav perching,” in *AIAA Guidance, Navigation and Control Conference and Exhibit*, 2008.
- [3] M. Kovač, J. Germann, C. Hürzeler, R. Y. Siegwart, and D. Floreano, “A perching mechanism for micro aerial vehicles,” *Journal of Micro-Nano Mechatronics*, 2009.
- [4] A. Lussier Desbiens, A. T. Asbeck, and M. R. Cutkosky, “Landing, perching and taking off from vertical surfaces,” *The International Journal of Robotics Research*, 2011.
- [5] D. Mehanovic, D. Rancourt, and A. L. Desbiens, “Fast and efficient aerial climbing of vertical surfaces using fixed-wing uavs,” *IEEE Robotics and Automation Letters*, 2018.
- [6] J. Moore and R. Tedrake, “Powerline perching with a fixed-wing uav,” in *AIAA Infotech@ Aerospace Conference and AIAA Unmanned... Unlimited Conference*, 2009.
- [7] X. Huang, Q. Xu, and J. Wang, “Vision-based autonomous landing of uav on moving platform using a new marker,” in *IOP Conference Series: Materials Science and Engineering*, 2019.
- [8] X. Yang, T. Wang, J. Liang, G. Yao, and M. Liu, “Survey on the novel hybrid aquatic-aerial amphibious aircraft,” *Progress in Aerospace Sciences*, 2015.
- [9] R. D. Eubank, “Autonomous flight, fault, and energy management of the flying fish solar-powered seaplane.” Ph.D. dissertation, The University of Michigan, 2012.
- [10] (2018) Gull uav : Capabilities. Warrior (Aero-Marine). [Online]. Available: <http://www.warrioraero.com/GULL/capabilities.htm>
- [11] (2006) Oregon iron works, inc. successfully completes first auto-landing test of unmanned seaplane. Business Wire. [Online]. Available: <https://www.tmcnet.com/usubmit/2006/05/30/1662493.htm>
- [12] R. Siddall and M. Kovač, “Launching the aquamav: bioinspired design for aerial-aquatic robotic platforms,” *Bioinspiration & biomimetics*, 2014.
- [13] R. Pelloquin, D. Thibault, and A. L. Desbiens, “Design of a Passive Vertical Takeoff and Landing Aquatic UAV,” *IEEE Robotics and Automation Letters*, 2017.
- [14] A. A. Neto, L. A. Mozelli, P. L. Drews, and M. F. Campos, “Attitude control for an hybrid unmanned aerial underwater vehicle: A robust switched strategy with global stability,” in *2015 IEEE International Conference on Robotics and Automation (ICRA)*, 2015.
- [15] M. M. Maia, P. Soni, and F. J. Diez, “Demonstration of an aerial and submersible vehicle capable of flight and underwater navigation with seamless air-water transition,” *arXiv preprint arXiv:1507.01932*, 2015.
- [16] D. Lu, C. Xiong, Z. Zeng, and L. Lian, “A multimodal aerial underwater vehicle with extended endurance and capabilities,” in *2019 International Conference on Robotics and Automation (ICRA)*, 2019.
- [17] W. Wang, J. Zhu, and M. Kuang, “Design, modelling and hovering control of a tail-sitter with single thrust-vectoring propeller,” in *2017 IEEE/RSJ International Conference on Intelligent Robots and Systems (IROS)*, 2017.
- [18] (2020) pixhawk®. pixhawk®. [Online]. Available: <https://pixhawk.org/>
- [19] (2020) Px4 autopilot. PX4 Autopilot. [Online]. Available: <https://px4.io/>
- [20] W. Phillips, *Mechanics of Flight*, ser. Engineering case studies online. Wiley, 2004. [Online]. Available: [https://books.google.ca/books?id=6-\\\_iGbjHM-8C](https://books.google.ca/books?id=6-\_iGbjHM-8C)
- [21] (2020) Motiongenesis™. MotionGenesis™. [Online]. Available: <http://www.motiongenesis.com/>
- [22] (2020) Series 1580/1585 thrust stand and dynamometer. RcBenchmark. [Online]. Available: <https://www.rcbenchmark.com/pages/series-1580-thrust-stand-dynamometer>
- [23] W. Khan and M. Nahon, “Modeling dynamics of agile fixed-wing uavs for real-time applications,” in *2016 international conference on unmanned aircraft systems (ICUAS)*, 2016.
- [24] (2019) Xflr5. XFRL5. [Online]. Available: <http://www.xflr5.tech/xflr5.htm>